On the rise and fall of Earth's strong clear-sky hemispheric albedo asymmetry

Michael S. Diamond[1,2,*], Jake J. Gristey[1,2], Jennifer E. Kay[1], & Graham Feingold[2]

1. Cooperative Institute for Research in Environmental Sciences, University of Colorado, Boulder, CO 80309, USA
2. NOAA Chemical Sciences Laboratory, Boulder, CO 80305, USA

*Email: michael.diamond@noaa.gov

Abstract

A striking feature of the Earth system is that the Northern and Southern Hemispheres reflect identical amounts of sunlight[1-5]. This hemispheric albedo symmetry comprises two asymmetries: The Northern Hemisphere is more reflective in clear skies, whereas the Southern Hemisphere is cloudier. The traditional explanation is that the clear-sky asymmetry is primarily due to the relatively-bright continents being disproportionately located in the Northern Hemisphere. Here we show that this explanation is inadequate because the clear-sky asymmetry is dominated by atmospheric aerosol, not surface reflection, and the greater reflection from Northern Hemisphere land is largely offset by greater reflection from the Antarctic surface than the Arctic surface. Climate model simulations suggest that aerosol emissions since the pre-industrial era have driven a large increase in the clear-sky asymmetry that would reverse in future low-emission scenarios featuring rapid decarbonization and decreases in co-emitted aerosol. High-emission scenarios also show a decrease in asymmetry, but instead driven by declines in Northern Hemisphere ice and snow cover. Strong clear-sky hemispheric albedo asymmetry is therefore a transient, rather than fixed, feature of Earth's climate. If all-sky symmetry is maintained, compensating cloud changes would have uncertain but important implications for Earth's energy balance, the hydrological cycle, and atmosphere-ocean circulations.

Introduction

Ever since reliable space-based estimates of Earth's albedo (broadband shortwave reflectivity) became available in the mid-1960s, it has been observed that the Northern and Southern Hemispheres (NH and SH, respectively) reflect the same amount of sunlight to within measurement uncertainty[1,3,6]. Although this hemispheric albedo symmetry appears to be non-trivial in a statistical sense[2,4], at present there exists no generally-accepted physical explanation for how this symmetry is maintained (if indeed it is maintained). State-of-the-art global climate models do not systematically simulate hemispherically symmetric albedos[2,3,5,6], and despite initial findings[1], Earth's outgoing longwave radiation does not currently exhibit a similar degree of hemispheric symmetry[3,6]. Prior measurements may have been inaccurate, or the real situation may have changed as the NH warmed faster than the SH over the last several decades[7]. The hemispheric imbalance in longwave radiation is balanced by cross-equatorial heat transport, with a northward oceanic heat transport driven by the Atlantic Meridional Overturning Circulation

partially offset by southward atmospheric heat transport associated with the northward location of the mean Intertropical Convergence Zone (ITCZ)[6,8-10].

Although the all-sky albedo is symmetrical between the hemispheres, its clear-sky and overcast components are markedly asymmetric, with much greater clear-sky reflection in the NH balanced by more abundant and brighter clouds in the SH, particularly in the midlatitudes[4,11,12]. The traditional explanation for the greater NH clear-sky reflection has to do with the arrangement of the continents: because land surfaces are brighter than the oceans, and most of the continents are in the NH, the NH clear-sky should be brighter than the SH. This hypothesis is supported by utilizing the spectral dimension of albedo to attribute the changes to Earth system properties[13]: the NH is brighter at near-infrared wavelengths associated with reflection from land surfaces and vegetation, whereas the SH is brighter at the visible wavelengths associated with reflection from clouds[3]. In this limited view, the NH clear-sky advantage should be stable on geological (millions of years) timescales.

However, the continent-based explanation of Earth's clear-sky hemispheric albedo asymmetry alone is, if not quite incorrect, substantially incomplete. To start, the atmospheric component of the NH-SH clear-sky asymmetry is larger than the surface component[3,5]. Here, we will show that the NH clear-sky atmospheric advantage is consistent with the hemispheric contrast in aerosol (airborne particulate matter). Additionally, the traditional view neglects the role of the cryosphere, which we will also show plays an important role in setting Earth's clear-sky albedo contrast at the surface. If the atmosphere and cryosphere matter for Earth's clear-sky hemispheric albedo asymmetry, the clear-sky asymmetry is more ephemeral than previously recognized. And if clouds adjust to maintain all-sky albedo symmetry, then a changing clear-sky asymmetry would have hard-to-predict ripple effects across the climate system.

Results

Atmosphere and cryosphere controls on clear-sky hemispheric albedo asymmetry

To assess the atmospheric and surface contributions to Earth's observed clear-sky albedo, we separate these components in the Clouds and the Earth's Radiant Energy System (CERES) Energy Balanced and Filled (EBAF) product[14,15] using a simple single-layer model of shortwave radiative transfer[16-18] (see Methods). Global maps of total clear-sky reflected shortwave radiation (R_{clr}) and its atmospheric and surface contributions are shown in Extended Data Figures 1, 2a, and 3a. Ocean surfaces are extremely dark whereas land is generally brighter, with ice and desert surfaces in particular reflecting very large quantities of sunlight. Reflection from the atmosphere is more globally uniform, although clear maxima are evident in areas of high aerosol concentration (e.g., East Asia, Sahara outflow). Regions of high topography (e.g., the Andes, Tibet, Antarctica) have minima in atmospheric reflection due to the simple mechanics of there being a thinner overlying atmosphere than in regions closer to sea-level.

Figure 1 shows this clear-sky decomposition averaged over each hemisphere, as the average NH minus SH difference (ΔR_{clr}), and as the NH-SH difference zonally. In each hemisphere, the atmosphere contributes approximately 60% of the total clear-sky reflection and the surface

approximately 40%. However, the atmosphere contributes approximately 80% of the hemispheric contrast, with the surface only contributing 20%.

If the continents are mostly located in the NH, and are brighter than the ocean, what can account for such a small surface contribution to the clear-sky hemispheric albedo asymmetry? The answer is: compensation by the cryosphere, specifically by Antarctica. As can be seen from the zonal surface contribution in Figure 1c, the NH continental advantage is substantial from the tropics to the midlatitudes. At around 60°, however, the situation reverses dramatically, with the Antarctic reflecting so much more sunlight than the Arctic that a large portion (~4 W/m^2) of the lower latitude continent-based advantage (~5.5 W/m^2) is erased. In contrast, the NH atmosphere is more reflective at all latitudes, with peaks in the tropics and poles (related in part to the mechanical effect of Antarctica's high topography).

To better understand the atmospheric component of the clear-sky reflection asymmetry, we analyze total aerosol optical depth (AOD or τ_a) and its contributions from black carbon (BC), dust, organic carbon (OC), sea salt, and sulfate (SO$_4$) aerosols in the Modern-Era Retrospective analysis for Research and Applications, Version 2 (MERRA-2) product[19-21] (Fig. 1d; see Methods).

The NH dominates AOD in the tropics primarily through a large dust contribution. In the midlatitudes, sulfate pollution in the NH largely balances sea salt in the SH. Without the (largely anthropogenic) sulfate contribution, the SH would presumably dominate midlatitude AOD. Carbonaceous aerosols (mainly OC) slightly favor the SH in the tropics and the NH closer to the poles. Since dust and sea salt aerosol are largely "natural" in origin, whereas sulfate is largely due to industrial emissions, it is reasonable to expect that the hemispheric AOD contrast ($\Delta\tau_a$) — and therefore atmospheric ΔR_{clr} — may have been substantially milder in the pre-industrial climate.

From a cleaner past...

To test this idea, we analyze output from seven coupled climate models that participated in the Aerosol Chemistry Model Intercomparison Project (AerChemMIP)[22] "hist-piAer" experiment, in which aerosol precursor emissions[23] are kept at pre-industrial (PI) values but all else evolves in the same manner as the "historical" experiment (see Methods). Figure 2 shows the clear-sky hemispheric albedo asymmetry and its atmospheric and surface contributions from 1850-1865 and 2000-2015 for the historical simulations and from 2000-2015 for the hist-piAer simulations.

For the present-day (PD) period (2000-2015), the models vary by a few W/m^2 in terms of their total clear-sky asymmetries, but diverge more radically from the observations in their breakdown between atmospheric and surface reflection (Fig. 2a-c). No model matches the observed dominance of the atmospheric component over the surface, and some (e.g., MIROC6 and NorESM2-LM) have the ratio reversed as compared to CERES. Extended Data Figures 2-4 show the difference in R_{clr} (model minus CERES) for the atmosphere ($R_{clr,atm}$) and surface ($R_{clr,sfc}$) globally and as averaged over tropical, midlatitude, and polar latitude bands, respectively. The underestimates in atmospheric R_{clr} (Extended Data Fig. 2) are mainly in the tropics (particularly over South America, Africa, and Arabia) and NH midlatitudes (particularly over eastern North

America and Europe) and the overestimates in surface R_{clr} (Extended Data Fig. 3) are concentrated over the continents. For MIROC6 in particular, dramatic biases in Antarctic sea ice (Extended Data Fig. 3e) help explain its anomalously low SH surface reflectance (Fig. 2c).

These biases notwithstanding, it is apparent that the atmospheric component of the clear-sky albedo symmetry was much lower (~50-100%) in the PI era (Fig. 2e) or with PI aerosol precursors (Fig. 2h) in the models. [This is partially offset in the total asymmetry by declining NH snow and sea ice cover in the historical PD-PI comparisons (Fig. 2d).] Using GISS-E2-1-G as an example (Fig. 2j-l), timeseries of the full historical and hist-piAer simulations show that the divergence in the experiments (toward greater asymmetry in the historical total and atmospheric R_{clr}) takes off around the Second World War period (~1935-1950) and is largely complete by the 1960s and 1970s — which happens to be the earliest time period in which we have space-based observations of Earth's albedo. It is thus possible that we only have reliable observations starting from a relatively unusual time for Earth's clear-sky albedo asymmetry.

The model asymmetry in AOD is highly correlated (Pearson's $r = 0.93$) with the asymmetry in the atmospheric component of R_{clr} (Fig. 3), consistent with a leading role of aerosol in driving variability in $R_{clr,atm}$ over space and time. However, CERES/MERRA-2 values are an outlier compared to the model-based regression fit (see Methods). The fit based on interannual variability in the asymmetries from CERES and MERRA-2 suggests a much steeper increase in $\Delta R_{clr,atm}$ for an increase in $\Delta\tau_a$ than seen in the model ensemble. This is not likely due to the different method of calculating the fit: when comparing slopes calculated using only data from 2000-2015 versus for all years 1850-2015 in each model, there are no systematic differences (Extended Data Fig. 5). If we therefore assume that the CERES/MERRA-2 interannual slope is also representative of PD-PI differences, we can then estimate the PI value of the clear-sky atmospheric albedo asymmetry for a given PI aerosol asymmetry.

To estimate the PI aerosol asymmetry, we use the good correlation ($r = 0.87$) between the global mean AOD in the PD for a given model and its PD-PI change in $\Delta\tau_a$ (Extended Data Fig. 6) as an emergent constraint. Via Monte Carlo simulation (see Methods), we find that the PI value of $\Delta R_{clr,atm}$ was 2.4 W/m^2 (95% confidence interval of 0.7 W/m^2 to 3.9 W/m^2), around half the PD value of 4.9 ± 0.4 W/m^2. This would represent a substantial decrease in the total clear-sky hemispheric albedo asymmetry in the PI compared to that observed today.

...toward either a less polluted or less icy future

If the past had weaker contrast than the present, what about the future? Under very different future scenarios within the Shared Socioeconomic Pathways (SSPs)[24,25] there is one consistent outcome: the clear-sky hemispheric albedo asymmetry is projected to decline in the coming century (Fig. 4).

For the low-emission SSP1-2.6 ("sustainability") scenario, the atmospheric component of R_{clr} drives a decline in overall asymmetry (Fig. 4ab) while the surface plays a more minor role (Fig. 4c), consistent with a decline in co-emitted aerosols and precursor gases. In contrast, the high-emission SSP3-7.0 ("regional rivalry") scenario gets the same overall result (Fig. 4g) but driven by the surface (Fig. 4i), rather than the atmosphere (Fig. 4h), consistent with maintained high

emissions of aerosols and their precursors. Results for the intermediate SSP2-4.5 ("middle of the road") scenario are, fittingly, a blend of those from the two other scenarios (Fig. 4d-f). As illustrated by the UKESM1-0-LL results (Fig. 4j-l), the divergence in the scenarios is apparent by midcentury.

The surface changes in SSP3-7.0 are largely a story of sea ice (Fig. 5). The hemispheric contrast in sea ice area (see Methods) has a good correlation ($r = 0.77$) with the hemispheric contrast in the surface component of R_{clr}. All models show a decline in Arctic sea ice and NH snow and ice cover on land with warming, but the magnitude and even sign of Antarctic sea ice changes are more variable (Extended Data Fig. 7). This is in part a mean state issue: models like MIROC6 and NorESM2-LM that have small amounts of Antarctic sea ice in the present day (Extended Data Fig. 3e,g) have limited room for future declines.

Changes in sea ice albedo[26] and in snow and ice cover on land[27] may also factor into the surface asymmetry changes. For instance, despite nearly equally-balanced trends in NH and SH sea ice area in MRI-ESM2-0 (Fig. 5, Extended Data Fig. 7e,l), there is a modest decline in surface asymmetry associated with decreased reflection over northern and western North America and the Himalayan highlands and Tibetan Plateau.

Due to large internal variability in sea ice concentration[28-30] and outstanding questions about sea ice dynamics, particularly in the Antarctic[31-34], how the surface component of the clear-sky albedo asymmetry would change in reality in a high-warming scenario is subject to more uncertainty than the aerosol-driven atmospheric component. However, it is very plausible that the $R_{clr,sfc}$ asymmetry could substantially decline and even reverse in the future if Arctic sea ice and NH land snow and ice cover are lost more rapidly than Antarctic sea ice in a warming climate.

Discussion

The changing nature of Earth's clear-sky albedo asymmetry should be observable in the coming decades under any of the future scenarios considered, especially with the planned launch of several visible-shortwave infrared spectroradiometers that will allow for spectral decomposition of reflected sunlight[35]. We run simplified radiative transfer simulations (see Methods) to investigate the spectral signal of a decrease in Northern Hemisphere aerosol loading (Extended Data Fig. 8). A cleaner Northern Hemisphere becomes less reflective in the visible spectrum (more associated with reflection from the atmosphere) but has a smaller change in the near-infrared (more associated with reflection from the land surface and vegetation) for all but the highest solar zenith angles. This will exacerbate the present hemispheric differences in the visible and near-infrared reflection[2], which will be directly observed during the upcoming Earth radiation budget satellite mission, Libera.

It is tempting to think that we may have glimpsed a lower aerosol and clear-sky asymmetry future during 2020 as a result of the societal response to the COVID-19 pandemic[36,37]. Indeed, 2020 featured low outliers in clear-sky hemispheric albedo asymmetry and aerosol contrast values (Fig. 2j-k, Fig. 3, Fig. 4j-k). However, the aerosol changes associated with the pandemic

lockdowns and economic slowdown were likely too small to be clearly distinguishable above background variability[38-40] and 2020 also featured anomalously large aerosol loadings over the Southern Ocean from the 2019-2020 Australian bushfires[41]. Future work is merited to better understand the unique conditions in 2020.

If clouds respond to the changing clear-sky contrast to maintain all-sky symmetry, there would be important implications for radiative forcing and hydrological and circulation changes depending on the (currently unknown) adjustment mechanism. If SH clouds darken to compensate for the NH trend, the resulting positive radiative forcing would accelerate global warming. Some worrying evidence that such a hemispheric connection exists comes from CERES reflected shortwave measurements over the past two decades that show nearly equal all-sky darkening trends in the NH and SH[4,42,43]. A strong decline in cloudiness within the northeastern Pacific stratocumulus deck and reductions in aerosol from eastern North America and eastern Asia offer an explanation for the NH trends[43-45], but there is no clear driver for the identical SH trend[4]. Alternatively, if NH clouds brighten to compensate for the clear-sky darkening, global radiative implications could be minor. Of course, the true response (if any) may involve some combination of both NH cloud brightening and SH darkening.

One hypothesized adjustment mechanism involves shifts in the ITCZ and thus tropical cloudiness toward the darker hemisphere[46]. If this were to occur, it would have important regional implications beyond the global mean precipitation shift[47], particularly for drought-vulnerable locations like the Sahel[48-50]. More recently, attention has shifted to the role played by the extremely cloudy SH midlatitude oceans[4,5]. Changes in Southern Ocean cloudiness could affect large-scale atmosphere-ocean circulations[12,51-53] and long-term global warming via changes in ocean heat uptake in the Southern Ocean[54-56]. Given the likelihood of large changes in the clear-sky hemispheric albedo asymmetry this century under any plausible emissions scenario, determining which of these or other as-yet-unidentified mechanisms would likely operate to maintain the all-sky hemispheric albedo symmetry should be a research priority.

References

1   Vonder Haar, T. H. & Suomi, V. E. Measurements of the Earth's Radiation Budget from Satellites During a Five-Year Period. Part I: Extended Time and Space Means. *Journal of Atmospheric Sciences* **28**, 305-314, doi:10.1175/1520-0469(1971)028<0305:Moterb>2.0.Co;2 (1971).
2   Voigt, A., Stevens, B., Bader, J. & Mauritsen, T. The Observed Hemispheric Symmetry in Reflected Shortwave Irradiance. *Journal of Climate* **26**, 468-477, doi:10.1175/jcli-d-12-00132.1 (2013).
3   Stephens, G. L. *et al.* The albedo of Earth. *Reviews of Geophysics* **53**, 141-163, doi:10.1002/2014rg000449 (2015).
4   Datseris, G. & Stevens, B. Earth's Albedo and Its Symmetry. *AGU Advances* **2**, doi:10.1029/2021av000440 (2021).
5   Jönsson, A. & Bender, F. A. M. Persistence and variability of Earth's inter-hemispheric albedo symmetry in 19 years of CERES EBAF observations. *Journal of Climate*, 1-62, doi:10.1175/jcli-d-20-0970.1 (2021).

6   Stephens, G. L. *et al.* The Curious Nature of the Hemispheric Symmetry of the Earth's Water and Energy Balances. *Current Climate Change Reports* **2**, 135-147, doi:10.1007/s40641-016-0043-9 (2016).

7   Friedman, A. R., Hwang, Y.-T., Chiang, J. C. H. & Frierson, D. M. W. Interhemispheric Temperature Asymmetry over the Twentieth Century and in Future Projections. *Journal of Climate* **26**, 5419-5433, doi:10.1175/jcli-d-12-00525.1 (2013).

8   Frierson, D. M. W. *et al.* Contribution of ocean overturning circulation to tropical rainfall peak in the Northern Hemisphere. *Nature Geoscience* **6**, 940-944, doi:10.1038/ngeo1987 (2013).

9   Marshall, J., Donohoe, A., Ferreira, D. & McGee, D. The ocean's role in setting the mean position of the Inter-Tropical Convergence Zone. *Climate Dynamics* **42**, 1967-1979, doi:10.1007/s00382-013-1767-z (2013).

10   Loeb, N. G. *et al.* Observational constraints on atmospheric and oceanic cross-equatorial heat transports: revisiting the precipitation asymmetry problem in climate models. *Climate Dynamics* **46**, 3239-3257, doi:10.1007/s00382-015-2766-z (2016).

11   Bender, F. A. M., Engström, A., Wood, R. & Charlson, R. J. Evaluation of Hemispheric Asymmetries in Marine Cloud Radiative Properties. *Journal of Climate* **30**, 4131-4147, doi:10.1175/jcli-d-16-0263.1 (2017).

12   Kay, J. E. *et al.* Global Climate Impacts of Fixing the Southern Ocean Shortwave Radiation Bias in the Community Earth System Model (CESM). *Journal of Climate* **29**, 4617-4636, doi:10.1175/jcli-d-15-0358.1 (2016).

13   Gristey, J. J. *et al.* Shortwave Spectral Radiative Signatures and Their Physical Controls. *Journal of Climate* **32**, 4805-4828, doi:10.1175/jcli-d-18-0815.1 (2019).

14   Loeb, N. G. *et al.* Clouds and the Earth's Radiant Energy System (CERES) Energy Balanced and Filled (EBAF) Top-of-Atmosphere (TOA) Edition-4.0 Data Product. *Journal of Climate* **31**, 895-918, doi:10.1175/jcli-d-17-0208.1 (2018).

15   Kato, S. *et al.* Surface Irradiances of Edition 4.0 Clouds and the Earth's Radiant Energy System (CERES) Energy Balanced and Filled (EBAF) Data Product. *Journal of Climate* **31**, 4501-4527, doi:10.1175/jcli-d-17-0523.1 (2018).

16   Donohoe, A. & Battisti, D. S. Atmospheric and Surface Contributions to Planetary Albedo. *Journal of Climate* **24**, 4402-4418, doi:10.1175/2011jcli3946.1 (2011).

17   Qu, X. & Hall, A. Surface Contribution to Planetary Albedo Variability in Cryosphere Regions. *Journal of Climate* **18**, 5239-5252, doi:10.1175/jcli3555.1 (2005).

18   Diamond, M. S., Director, H. M., Eastman, R., Possner, A. & Wood, R. Substantial Cloud Brightening from Shipping in Subtropical Low Clouds. *AGU Advances* **1**, e2019AV000111, doi:10.1029/2019av000111 (2020).

19   Gelaro, R. *et al.* The Modern-Era Retrospective Analysis for Research and Applications, Version 2 (MERRA-2). *Journal of Climate* **30**, 5419-5454, doi:10.1175/jcli-d-16-0758.1 (2017).

20   Randles, C. A. *et al.* The MERRA-2 Aerosol Reanalysis, 1980 - onward, Part I: System Description and Data Assimilation Evaluation. *Journal of Climate* **30**, 6823-6850, doi:10.1175/JCLI-D-16-0609.1 (2017).

21   Buchard, V. *et al.* The MERRA-2 Aerosol Reanalysis, 1980 Onward. Part II: Evaluation and Case Studies. *Journal of Climate* **30**, 6851-6872, doi:10.1175/jcli-d-16-0613.1 (2017).

22   Collins, W. J. *et al.* AerChemMIP: quantifying the effects of chemistry and aerosols in CMIP6. *Geosci. Model Dev.* **10**, 585-607, doi:10.5194/gmd-10-585-2017 (2017).

23   Feng, L. *et al.* The generation of gridded emissions data for CMIP6. *Geosci. Model Dev.* **13**, 461-482, doi:10.5194/gmd-13-461-2020 (2020).

24   Riahi, K. *et al.* The Shared Socioeconomic Pathways and their energy, land use, and greenhouse gas emissions implications: An overview. *Global Environmental Change* **42**, 153-168, doi:10.1016/j.gloenvcha.2016.05.009 (2017).

25   O'Neill, B. C. *et al.* The Scenario Model Intercomparison Project (ScenarioMIP) for CMIP6. *Geosci. Model Dev.* **9**, 3461-3482, doi:10.5194/gmd-9-3461-2016 (2016).

26   Pistone, K., Eisenman, I. & Ramanathan, V. Observational determination of albedo decrease caused by vanishing Arctic sea ice. *Proc Natl Acad Sci U S A* **111**, 3322-3326, doi:10.1073/pnas.1318201111 (2014).

27   Bormann, K. J., Brown, R. D., Derksen, C. & Painter, T. H. Estimating snow-cover trends from space. *Nature Climate Change* **8**, 924-928, doi:10.1038/s41558-018-0318-3 (2018).

28   Swart, N. C., Fyfe, J. C., Hawkins, E., Kay, J. E. & Jahn, A. Influence of internal variability on Arctic sea-ice trends. *Nature Climate Change* **5**, 86-89, doi:10.1038/nclimate2483 (2015).

29   Kay, J. E., Holland, M. M. & Jahn, A. Inter-annual to multi-decadal Arctic sea ice extent trends in a warming world. *Geophysical Research Letters* **38**, doi:10.1029/2011gl048008 (2011).

30   Singh, H. A., Polvani, L. M. & Rasch, P. J. Antarctic Sea Ice Expansion, Driven by Internal Variability, in the Presence of Increasing Atmospheric CO2. *Geophysical Research Letters* **46**, 14762-14771, doi:10.1029/2019gl083758 (2019).

31   Sun, S. & Eisenman, I. Observed Antarctic sea ice expansion reproduced in a climate model after correcting biases in sea ice drift velocity. *Nat Commun* **12**, 1060, doi:10.1038/s41467-021-21412-z (2021).

32   Eayrs, C., Li, X., Raphael, M. N. & Holland, D. M. Rapid decline in Antarctic sea ice in recent years hints at future change. *Nature Geoscience* **14**, 460-464, doi:10.1038/s41561-021-00768-3 (2021).

33   Parkinson, C. L. & Cavalieri, D. J. Antarctic sea ice variability and trends, 1979-2010. *The Cryosphere* **6**, 871-880, doi:10.5194/tc-6-871-2012 (2012).

34   Comiso, J. C. *et al.* Positive Trend in the Antarctic Sea Ice Cover and Associated Changes in Surface Temperature. *J Clim* **30**, 2251-2267, doi:10.1175/jcli-d-16-0408.1 (2017).

35   Stephens, G. *et al.* The Spectral Nature of Earth's Reflected Radiation: Measurement and Science Applications. *Frontiers in Remote Sensing* **2**, doi:10.3389/frsen.2021.664291 (2021).

36   Wang, C., Horby, P. W., Hayden, F. G. & Gao, G. F. A novel coronavirus outbreak of global health concern. *The Lancet* **395**, 470-473, doi:10.1016/s0140-6736(20)30185-9 (2020).

37   Tian, H. *et al.* An investigation of transmission control measures during the first 50 days of the COVID-19 epidemic in China. *Science* **368**, 638-642, doi:10.1126/science.abb6105 (2020).

38   Diamond, M. S. & Wood, R. Limited Regional Aerosol and Cloud Microphysical Changes Despite Unprecedented Decline in Nitrogen Oxide Pollution During the

February 2020 COVID-19 Shutdown in China. *Geophysical Research Letters* **47**, e2020GL088913, doi:10.1029/2020gl088913 (2020).

39   Gettelman, A., Lamboll, R., Bardeen, C. G., Forster, P. M. & Watson-Parris, D. Climate Impacts of COVID-19 Induced Emission Changes. *Geophysical Research Letters* **48**, doi:10.1029/2020gl091805 (2021).

40   Jones, C. D. *et al.* The Climate Response to Emissions Reductions Due to COVID-19: Initial Results From CovidMIP. *Geophysical Research Letters* **48**, doi:10.1029/2020gl091883 (2021).

41   Hirsch, E. & Koren, I. Record-breaking aerosol levels explained by smoke injection into the stratosphere. *Science* **371**, 1269-1274, doi:10.1126/science.abe1415 (2021).

42   Loeb, N. G. *et al.* Satellite and Ocean Data Reveal Marked Increase in Earth's Heating Rate. *Geophysical Research Letters* **48**, doi:10.1029/2021gl093047 (2021).

43   Raghuraman, S. P., Paynter, D. & Ramaswamy, V. Anthropogenic forcing and response yield observed positive trend in Earth's energy imbalance. *Nat Commun* **12**, 4577, doi:10.1038/s41467-021-24544-4 (2021).

44   Loeb, N., Thorsen, T., Norris, J., Wang, H. & Su, W. Changes in Earth's Energy Budget during and after the "Pause" in Global Warming: An Observational Perspective. *Climate* **6**, doi:10.3390/cli6030062 (2018).

45   Andersen, H., Cermak, J., Zipfel, L. & Myers, T. A. Attribution of Observed Recent Decrease in Low Clouds Over the Northeastern Pacific to Cloud-Controlling Factors. *Geophysical Research Letters* **49**, doi:10.1029/2021gl096498 (2022).

46   Voigt, A., Stevens, B., Bader, J. & Mauritsen, T. Compensation of Hemispheric Albedo Asymmetries by Shifts of the ITCZ and Tropical Clouds. *Journal of Climate* **27**, 1029-1045, doi:10.1175/jcli-d-13-00205.1 (2014).

47   Atwood, A. R., Donohoe, A., Battisti, D. S., Liu, X. & Pausata, F. S. R. Robust Longitudinally Variable Responses of the ITCZ to a Myriad of Climate Forcings. *Geophysical Research Letters* **47**, doi:10.1029/2020gl088833 (2020).

48   Zhang, S., Stier, P., Dagan, G. & Wang, M. Anthropogenic Aerosols Modulated 20th-Century Sahel Rainfall Variability Via Their Impacts on North Atlantic Sea Surface Temperature. *Geophysical Research Letters* **49**, doi:10.1029/2021gl095629 (2021).

49   Allen, R. J., Evan, A. T. & Booth, B. B. B. Interhemispheric Aerosol Radiative Forcing and Tropical Precipitation Shifts during the Late Twentieth Century. *Journal of Climate* **28**, 8219-8246, doi:10.1175/jcli-d-15-0148.1 (2015).

50   Marvel, K., Biasutti, M. & Bonfils, C. Fingerprints of external forcings on Sahel rainfall: aerosols, greenhouse gases, and model-observation discrepancies. *Environmental Research Letters* **15**, doi:10.1088/1748-9326/ab858e (2020).

51   Kang, S. M., Held, I. M., Frierson, D. M. W. & Zhao, M. The Response of the ITCZ to Extratropical Thermal Forcing: Idealized Slab-Ocean Experiments with a GCM. *Journal of Climate* **21**, 3521-3532, doi:10.1175/2007jcli2146.1 (2008).

52   Hwang, Y. T. & Frierson, D. M. Link between the double-Intertropical Convergence Zone problem and cloud biases over the Southern Ocean. *Proc Natl Acad Sci U S A* **110**, 4935-4940, doi:10.1073/pnas.1213302110 (2013).

53   Kang, S. M. *et al.* Extratropical–Tropical Interaction Model Intercomparison Project (Etin-Mip): Protocol and Initial Results. *Bulletin of the American Meteorological Society* **100**, 2589-2606, doi:10.1175/bams-d-18-0301.1 (2019).

54   Frey, W. R., Maroon, E. A., Pendergrass, A. G. & Kay, J. E. Do Southern Ocean Cloud Feedbacks Matter for 21st Century Warming? *Geophysical Research Letters* **44**, 12,447-412,456, doi:10.1002/2017GL076339 (2017).

55   Gjermundsen, A. *et al.* Shutdown of Southern Ocean convection controls long-term greenhouse gas-induced warming. *Nature Geoscience* **14**, 724-731, doi:10.1038/s41561-021-00825-x (2021).

56   Morrison, A. L., Singh, H. A. & Rasch, P. J. Observations Indicate That Clouds Amplify Mechanisms of Southern Ocean Heat Uptake. *Journal of Geophysical Research: Atmospheres* **127**, doi:10.1029/2021jd035487 (2022).

Methods

Reflected shortwave radiation data

Clear-sky shortwave fluxes from January 2003 to December 2020 come from CERES EBAF Edition 4.1 and are estimated for the total region (including both cloudy and clear scenes) rather than for only cloud-free portions of scenes[14]. Clear-sky fluxes estimated in this manner are more comparable with clear-sky output from climate models. Results using clear-sky fluxes from cloud-free portions of scenes only are qualitatively similar to those shown here.

CERES instruments measure filtered radiances in the shortwave spectrum from 0.3 to 5 µm and fly aboard NASA's polar-orbiting Terra and Aqua satellites as well as the Suomi National Polar-Orbiting Partnership and NOAA-20 satellites[14]. We select data from 2003-2020 in which both Terra and Aqua measurements are available. Data from geostationary satellites are used to correct for the full diurnal cycle and a one-time adjustment (within the range of observational and calibration uncertainty) is applied to ensure that the measured net imbalance in top-of-atmosphere (TOA) radiation matches values from in situ observations of ocean heat uptake[14,57,58]. Surface irradiances are computed independently using aerosol, cloud, and thermodynamic properties from satellite observations and reanalysis products and constrained by the TOA irradiances[15].

Uncertainty in the temporal mean values discussed is quantified using the interannual variability assuming a red noise process[59]. Measurement uncertainties are neglected. This approach has the main advantage of allowing us to quantify uncertainty identically between the CERES observations and the CMIP6 models. It is justified because random measurement errors on the order of 1-10 W/m^2 per 1° x 1° monthly grid box[14,15] rapidly diminish when averaging hemispherically or globally for long time periods [errors of O(0.001-0.01 W/m^2) as compared to errors of O(0.1-1 W/m^2) for temporal averaging assuming red-noise] and while systematic errors would be more concerning in an absolute sense[16], they would not affect conclusions drawn on the atmosphere/surface breakdown or on hemispheric differences.

Spatiotemporal weighted averaging is performed accounting for the fact that months have slightly different lengths and that the Earth is oblate, not perfectly spherical. Failure to properly weight by days per month and area can result in errors of O(0.1 W/m^2) in globally and hemispherically averaged values.

Aerosol reanalysis data

Total AOD at 550 nm from MERRA-2 is constrained by assimilation of AOD as retrieved by the Moderate Resolution Imaging Spectroradiometer instrument aboard the Terra and Aqua satellites, in addition to several other satellite instruments and the AERONET ground sites, but the breakdown into different species is only constrained indirectly through the total AOD constraint[20]. We therefore place greater emphasis on and have greater confidence in the total AOD values than their species decomposition. MERRA-2 does compare well overall with unassimilated satellite and aircraft measurements of aerosol column optical properties and vertical extinction profiles, however, lending some greater confidence[21]. MERRA-2 AOD behaves similarly to other reanalysis products and generally compares well with various observational datasets[60], making it unlikely that the choice to focus on MERRA-2 as opposed to another equally suitable product has any bearing on our results or conclusions. Uncertainty in temporal mean values is quantified assuming red noise[59], as for the reflection data. MERRA-2 data is analyzed from January 2003 to December 2020 to match the CERES record.

Sea ice concentration data

Sea ice area data from passive microwave remote sensing observations from January 2003 to December 2020 come from the National Snow and Ice Data Center (NSIDC) Sea Ice Index Version 3 product[61]. Weighting sea ice area by insolation improves its correlation with $R_{\mathrm{clr,sfc}}$ for each hemisphere separately but has a negligible impact on the hemispheric difference.

Climate model data

Seven state-of-the-art global climate models (abbreviated names in parentheses) from the Coupled Model Intercomparison Project Phase 6 (CMIP6) archive[62] are selected based on their participation in the Aerosol Chemistry Model Intercomparison Project (AerChemMIP) hist-piAer experiment[22] and the Scenario Model Intercomparison Project (ScenarioMIP) SSP1-2.6, SSP2-4.5, and SSP3-7.0 experiments[25]: NOAA Geophysical Fluid Dynamics Laboratories GFDL-ESM4 (GFDL)[63-65]; NASA Goddard Institute for Space Studies GISS-E2-1-G (GISS)[66-68]; Institut Pierre-Simon Laplace IPSL-CM6A-LR (IPSL)[69-71]; University of Tokyo, National Institute for Environmental Studies, and Japan Agency for Marine-Earth Science and Technology MIROC6 (MIROC)[72-74]; Japan Meteorological Agency Meteorological Research Institute MRI-ESM2-0 (MRI)[75-77]; Norwegian Earth System Model Climate Modeling Consortium NorESM2-LM (NorESM)[78-80]; and the UK Met Office Hadley Centre-Natural Environment Research Council UKESM1-0-LL (UKESM)[81-83].

For models with multiple variants, only one is selected for analysis per model: r1i1p1f1 (GFDL, IPSL, MIROC6, MRI, NorESM); r1i1p3f1 (GISS); and r1i1p1f2 (UKESM).

Temporal averaging accounts for the different calendars (e.g., Gregorian versus uniform 30-day months) used by each model and spatial averaging uses atmospheric grid box area for the radiation and aerosol (AOD at 550 nm) fields and either the atmospheric or oceanic grid box area

for sea ice depending on the model and its archived output. Uncertainty in temporal means is calculated assuming a red noise process, as in the observations.

Decomposition of top-of-atmosphere reflection into atmospheric and surface components

Following Donohoe & Battisti[16] and Diamond et al.[18], we calculate the atmospheric component of the top-of-atmosphere (TOA) planetary albedo using the relation:

$$A = \alpha_{atm} + \alpha_{sfc} \frac{\mathcal{T}^2}{(1-\alpha_{atm}\alpha_{\text{sfc}})},$$

(1)

where A is the planetary albedo (calculated as the ratio of upwelling to downwelling shortwave radiation at TOA), α_{atm} is the atmospheric component of the planetary albedo, α_{sfc} is the surface albedo (calculated as the ratio of upwelling to downwelling shortwave radiation at the surface), and $\mathcal{T}$ is the atmospheric transmissivity (calculated as the ratio of downwelling radiation at the surface to that at TOA). We then calculate R_{clr} and its atmospheric and surface components ($R_{\text{clr,atm}}$ and $R_{\text{clr,sfc}}$, respectively) by multiplying by the incoming solar radiation flux, $F_\odot$:

$$R_{clr} = R_{clr,atm} + R_{clr,sfc} = F_\odot \alpha_{atm} + F_\odot \alpha_{sfc} \frac{\mathcal{T}^2}{(1-\alpha_{atm}\alpha_{\text{sfc}})}.$$

(2)

The atmosphere/surface reflection decomposition method is identical between the CERES observations and the CMIP6 models.

Pre-industrial aerosol contrast estimate

In order to calculate the PI value of the atmospheric component of the hemispheric asymmetry in R_{clr}, we need to estimate the PI value of the hemispheric AOD asymmetry and be able to relate the AOD and $R_{\text{clr,atm}}$ asymmetries.

To estimate the PI aerosol contrast, we use the ordinary least squares (OLS) regression between the PD value (defined as the 2000-2015 average) of global mean AOD and the difference between the hemispheric AOD asymmetry in the PD from the PI (defined as the 1850-1865 average) in the seven CMIP6 models as an emergent constraint (Extended Data Fig. 6). All averages are inclusive of the starting year and exclusive of the ending year (e.g., the 2000-2015 average includes all months from January 2000 to December 2014). Using the emergent constraint, we then estimate the real PI aerosol contrast using the PD global mean value from MERRA-2.

We use the OLS regression between $\Delta R_{\text{clr,atm}}$ from CERES and $\Delta\tau_a$ from MERRA-2 to estimate the PI value of the atmospheric component of the R_{clr} asymmetry. Based on the similarity between the 2000-2015 and 1850-2015 regressions from the CMIP6 models (Extended Data Fig. 5), the modern CERES-MERRA-2 relationship should be valid for extrapolation back to the PI era.

To quantify uncertainty, we use Monte Carlo simulation to generate 10,000 estimates by randomly drawing from t-distributions of the PD global mean AOD value from MERRA-2 (error calculated assuming red noise), the PD-PI difference in hemispheric AOD contrast (error calculated from the OLS regression uncertainty), the PD hemispheric contrast in AOD from MERRA-2 (error calculated assuming red noise) to calculate the PI hemispheric AOD contrast, and finally the PI value of the $R_{clr,atm}$ asymmetry (error calculated from the OLS regression uncertainty). Kernel density estimation of the Monte Carlo results is used for presentation purposes in Figure 3.

Spectral albedo calculations

Spectrally-resolved radiative transfer output used in Extended Data Figure 8 is calculated with 1D DIScrete Ordinate Radiative Transfer (DISORT) using the Santa Barbara DISORT Atmospheric Radiative Transfer (SBDART) program[84]. Calculations are performed from 0.2-3.0 µm at 0.005-µm spectral sampling. For simplicity, the NH and SH results are derived from a weighted combination of three calculations that each use standard surface and aerosol properties built into SBDART: (1) snow surface and tropospheric aerosol, (2) ocean surface and oceanic aerosol, and (3) vegetated surface and rural aerosol. The averaging weights for the NH/SH are (1) – 10%/10%, (2) – 58%/77%, and (3) – 32%/13%, respectively[4]. AOD is set to 0.2 for present day NH, 0.1 for present day SH, and 0.15 for clean NH. All calculations use the US Standard atmosphere.

Data availability

CERES data are available from the NASA Langley Research Center (https://ceres.larc.nasa.gov/data/). MERRA-2 data are available from the NASA Goddard Earth Sciences Data and Information Services Center (https://disc.gsfc.nasa.gov/datasets?project=MERRA-2). The Sea Ice Index is available from the NSIDC (https://nsidc.org/data/G02135/versions/3). CMIP6 data are available from the Earth System Grid Federation (ESGF) and were downloaded from the US Department of Energy/Lawrence Livermore National Laboratory node (https://esgf-node.llnl.gov/projects/cmip6/).

Code availability

All python libraries used in the analysis (cartopy[85], matplotlib[86], numpy[87], scipy[88], and xarray[89]) are freely available. The SBDART code is available from Paul Ricchiazzi (https://github.com/paulricchiazzi/SBDART).

Acknowledgements

Research Programme, which, through its Working Group on Coupled Modelling, coordinated and promoted CMIP6. We thank the climate modeling groups for producing and making available their model output, the ESGF for archiving the data and providing access, and the multiple funding agencies who support CMIP6 and ESGF. We thank Aiden Jönsson, Mike MacFerrin, Priyam Raghuraman Tim Smith, and Fangfang Yao for comments.

Author contributions

M.S.D. conceived and designed the study with input from J.J.G., J.E.K, and G.F. M.S.D. performed all analyses except for the radiative transfer calculations, which were performed by J.J.G. M.S.D. wrote the manuscript with input and editing from all coauthors.

Competing interests

The authors declare no competing interests.

Correspondence and requests for materials should be addressed to M.S.D.

Methods References

57   Loeb, N. G. *et al.* Toward Optimal Closure of the Earth's Top-of-Atmosphere Radiation Budget. *Journal of Climate* **22**, 748-766, doi:10.1175/2008jcli2637.1 (2009).

58   Johnson, G. C., Lyman, J. M. & Loeb, N. G. Improving estimates of Earth's energy imbalance. *Nature Climate Change* **6**, 639-640, doi:10.1038/nclimate3043 (2016).

59   Santer, B. D. *et al.* Statistical significance of trends and trend differences in layer-average atmospheric temperature time series. *Journal of Geophysical Research: Atmospheres* **105**, 7337-7356, doi:10.1029/1999jd901105 (2000).

60   Vogel, A. *et al.* Uncertainty in Aerosol Optical Depth From Modern Aerosol-Climate Models, Reanalyses, and Satellite Products. *Journal of Geophysical Research: Atmospheres* **127**, doi:10.1029/2021jd035483 (2022).

61   Fetterer, F., K. Knowles, W. N. Meier, M. Savoie & Windnagel., A. K.   (ed NSIDC: National Snow and Ice Data Center) (Boulder, Colorado USA, 2017, updated daily).

62   Eyring, V. *et al.* Overview of the Coupled Model Intercomparison Project Phase 6 (CMIP6) experimental design and organization. *Geoscientific Model Development* **9**, 1937-1958, doi:10.5194/gmd-9-1937-2016 (2016).

63   Krasting, J. P., John, J. G., Blanton, C., McHugh, C., Nikonov, S., Radhakrishnan, A., Rand, K., Zadeh, N. T., Balaji, V., Durachta, J., Dupuis, C., Menzel, R., Robinson, T., Underwood, S., Vahlenkamp, H., Dunne, K. A., Gauthier, P. P. G., Ginoux, P., Griffies, S. M., Hallberg, R., Harrison, M., Hurlin, W., Malyshev, S., Naik, V., Paulot, F., Paynter, D. J., Ploshay, J., Reichl, B. G., Schwarzkopf, D. M., Seman, C. J., Silvers, L., Wyman, B., Zeng, Y., Adcroft, A., Dunne, J. P., Dussin, R., Guo, H., He, J., Held, I. M., Horowitz, L. W., Lin, P., Milly, P. C. D., Shevliakova, E., Stock, C., Winton, M., Wittenberg, A. T., Xie, Y., and Zhao, M.: NOAA-GFDL GFDL-ESM4 model output prepared for CMIP6 CMIP historical (Version 20190806), Earth System Grid Federation [dataset], 10.22033/ESGF/CMIP6.8597, 2018.

64   Horowitz, L. W., Naik, V., Sentman, L., Paulot, F., Blanton, C., McHugh, C., Radhakrishnan, A., Rand, K., Vahlenkamp, H., Zadeh, N. T., Wilson, C., Ginoux, P., He, J., John, J. G., Lin, M., Paynter, D. J., Ploshay, J., Zhang, A., and Zeng, Y.: NOAA-GFDL GFDL-ESM4 model output prepared for CMIP6 AerChemMIP (Version 20190830), Earth System Grid Federation [dataset], 10.22033/ESGF/CMIP6.1404, 2018.

65   Guo, H., John, J. G., Blanton, C., McHugh, C., Nikonov, S., Radhakrishnan, A., Rand, K., Zadeh, N. T., Balaji, V., Durachta, J., Dupuis, C., Menzel, R., Robinson, T., Underwood, S., Vahlenkamp, H., Dunne, K. A., Gauthier, P. P. G., Ginoux, P., Griffies, S. M., Hallberg, R., Harrison, M., Hurlin, W., Lin, P., Malyshev, S., Naik, V., Paulot, F., Paynter, D. J., Ploshay, J., Schwarzkopf, D. M., Seman, C. J., Shao, A., Silvers, L., Wyman, B., Yan, X., Zeng, Y., Adcroft, A., Dunne, J. P., Held, I. M., Krasting, J. P., Horowitz, L. W., Milly, C., Shevliakova, E., Winton, M., Zhao, M., and Zhang, R.: NOAA-GFDL GFDL-CM4 model output prepared for CMIP6 ScenarioMIP (Version 20190618), Earth System Grid Federation [dataset], 10.22033/ESGF/CMIP6.9242, 2018.

66   NASA Goddard Institute for Space Studies (NASA/GISS): NASA-GISS GISS-E2.1G model output prepared for CMIP6 CMIP historical (Version 20191125), Earth System Grid Federation [dataset], 10.22033/ESGF/CMIP6.7127, 2018.

67   NASA Goddard Institute for Space Studies (NASA/GISS): NASA-GISS GISS-E2.1G model output prepared for CMIP6 AerChemMIP (Version 20200512), Earth System Grid Federation [dataset], 10.22033/ESGF/CMIP6.2059, 2019.

68   NASA Goddard Institute for Space Studies (NASA/GISS): NASA-GISS GISS-E2.1G model output prepared for CMIP6 ScenarioMIP (Version 20200127), Earth System Grid Federation [dataset], 10.22033/ESGF/CMIP6.2074, 2020.

69   Boucher, O., Denvil, S., Levavasseur, G., Cozic, A., Caubel, A., Foujols, M.-A., Meurdesoif, Y., Balkanski, Y., Checa-Garcia, R., Hauglustaine, D., Bekki, S., and Marchand, M.: IPSL IPSL-CM5A2-INCA model output prepared for CMIP6 CMIP historical (Version 20180711), Earth System Grid Federation [dataset], 10.22033/ESGF/CMIP6.13661, 2020.

70   Boucher, O., Denvil, S., Levavasseur, G., Cozic, A., Caubel, A., Foujols, M.-A., Meurdesoif, Y., Balkanski, Y., Checa-Garcia, R., Hauglustaine, D., Bekki, S., and Marchand, M.: IPSL IPSL-CM5A2-INCA model output prepared for CMIP6 AerChemMIP (20190109), Earth System Grid Federation [dataset], 10.22033/ESGF/CMIP6.13641, 2021.

71   Boucher, O., Denvil, S., Levavasseur, G., Cozic, A., Caubel, A., Foujols, M.-A., Meurdesoif, Y., Cadule, P., Devilliers, M., Dupont, E., and Lurton, T.: IPSL IPSL-CM5A2-INCA model output prepared for CMIP6 ScenarioMIP (Version 20181218), Earth System Grid Federation [dataset], 10.22033/ESGF/CMIP6.15667, 2020.

72   Tatebe, H. and Watanabe, M.: MIROC MIROC6 model output prepared for CMIP6 CMIP historical (Version 20190130), Earth System Grid Federation [dataset], 10.22033/ESGF/CMIP6.5603, 2018.

73   Takemura, T.: MIROC MIROC6 model output prepared for CMIP6 AerChemMIP (Version 20190801), Earth System Grid Federation [dataset], 10.22033/ESGF/CMIP6.9121, 2019.

74   Shiogama, H., Abe, M., and Tatebe, H.: MIROC MIROC6 model output prepared for CMIP6 ScenarioMIP (Version 20190612), Earth System Grid Federation [dataset], 10.22033/ESGF/CMIP6.898, 2019.

75   Yukimoto, S., Koshiro, T., Kawai, H., Oshima, N., Yoshida, K., Urakawa, S., Tsujino, H., Deushi, M., Tanaka, T., Hosaka, M., Yoshimura, H., Shindo, E., Mizuta, R., Ishii, M., Obata, A., and Adachi, Y.: MRI MRI-ESM2.0 model output prepared for CMIP6 CMIP historical (Version 20190220), Earth System Grid Federation [dataset], 10.22033/ESGF/CMIP6.6842, 2019.

76   Yukimoto, S., Koshiro, T., Kawai, H., Oshima, N., Yoshida, K., Urakawa, S., Tsujino, H., Deushi, M., Tanaka, T., Hosaka, M., Yoshimura, H., Shindo, E., Mizuta, R., Ishii, M., Obata, A., and Adachi, Y.: MRI MRI-ESM2.0 model output prepared for CMIP6 AerChemMIP (Version 20200828), Earth System Grid Federation [dataset], 10.22033/ESGF/CMIP6.633, 2019.

77   Yukimoto, S., Koshiro, T., Kawai, H., Oshima, N., Yoshida, K., Urakawa, S., Tsujino, H., Deushi, M., Tanaka, T., Hosaka, M., Yoshimura, H., Shindo, E., Mizuta, R., Ishii, M., Obata, A., and Adachi, Y.: MRI MRI-ESM2.0 model output prepared for CMIP6 ScenarioMIP (Version 20190220), Earth System Grid Federation [dataset], 10.22033/ESGF/CMIP6.638, 2019.

78   Seland, Ø., Bentsen, M., Oliviè, D. J. L., Toniazzo, T., Gjermundsen, A., Graff, L. S., Debernard, J. B., Gupta, A. K., He, Y., Kirkevåg, A., Schwinger, J., Tjiputra, J., Aas, K. S., Bethke, I., Fan, Y., Griesfeller, J., Grini, A., Guo, C., Ilicak, M., Karset, I. H. H., Landgren, O. A., Liakka, J., Moseid, K. O., Nummelin, A., Spensberger, C., Tang, H., Zhang, Z., Heinze, C., Iversen, T., and Schulz, M.: NCC NorESM2-LM model output prepared for CMIP6 CMIP historical (Version 20190815), Earth System Grid Federation [dataset], 10.22033/ESGF/CMIP6.8036, 2019.

79   Oliviè, D. J. L., Bentsen, M., Seland, Ø., Toniazzo, T., Gjermundsen, A., Graff, L. S., Debernard, J. B., Gupta, A. K., He, Y., Kirkevåg, A., Schwinger, J., Tjiputra, J., Aas, K. S., Bethke, I., Fan, Y., Griesfeller, J., Grini, A., Guo, C., Ilicak, M., Karset, I. H. H., Landgren, O. A., Liakka, J., Moseid, K. O., Nummelin, A., Spensberger, C., Tang, H., Zhang, Z., Heinze, C., Iversen, T., and Schulz, M.: NCC NorESM2-LM model output prepared for CMIP6 AerChemMIP (Version 20190818), Earth System Grid Federation [dataset], 10.22033/ESGF/CMIP6.574, 2019.

80   Seland, Ø., Bentsen, M., Oliviè, D. J. L., Toniazzo, T., Gjermundsen, A., Graff, L. S., Debernard, J. B., Gupta, A. K., He, Y., Kirkevåg, A., Schwinger, J., Tjiputra, J., Aas, K. S., Bethke, I., Fan, Y., Griesfeller, J., Grini, A., Guo, C., Ilicak, M., Karset, I. H. H., Landgren, O. A., Liakka, J., Moseid, K. O., Nummelin, A., Spensberger, C., Tang, H., Zhang, Z., Heinze, C., Iversen, T., and Schulz, M.: NCC NorESM2-LM model output prepared for CMIP6 ScenarioMIP (Version 20191206), Earth System Grid Federation [dataset], 10.22033/ESGF/CMIP6.604, 2019.

81   Tang, Y., Rumbold, S., Ellis, R., Kelley, D., Mulcahy, J., Sellar, A., Walton, J., and Jones, C.: MOHC UKESM1.0-LL model output prepared for CMIP6 CMIP historical (Version 20190405), Earth System Grid Federation [dataset], 10.22033/ESGF/CMIP6.6113, 2019.

82   O'Connor, F.: MOHC UKESM1.0-LL model output prepared for CMIP6 AerChemMIP (Version 20190809), Earth System Grid Federation [dataset], 10.22033/ESGF/CMIP6.1561, 2019.

83   Good, P., Sellar, A., Tang, Y., Rumbold, S., Ellis, R., Kelley, D., Kuhlbrodt, T., and Walton, J.: MOHC UKESM1.0-LL model output prepared for CMIP6 ScenarioMIP

(Version 20190723), Earth System Grid Federation [dataset], 10.22033/ESGF/CMIP6.1567, 2019.

84   Ricchiazzi, P., Yang, S., Gautier, C. & Sowle, D. SBDART: A Research and Teaching Software Tool for Plane-Parallel Radiative Transfer in the Earth's Atmosphere. *Bulletin of the American Meteorological Society* **79**, 2101-2114, doi:10.1175/1520-0477(1998)079<2101:Sarats>2.0.Co;2 (1998).

85   Cartopy: a cartographic python library with a matplotlib interface (Exeter, Devon, 2010-2015).

86   Hunter, J. D. Matplotlib: A 2D Graphics Environment. *Computing in Science & Engineering* **9**, 90-95, doi:10.1109/MCSE.2007.55 (2007).

87   Harris, C. R. *et al.* Array programming with NumPy. *Nature* **585**, 357-362, doi:10.1038/s41586-020-2649-2 (2020).

88   Virtanen, P. *et al.* SciPy 1.0: fundamental algorithms for scientific computing in Python. *Nat Methods* **17**, 261-272, doi:10.1038/s41592-019-0686-2 (2020).

89   Hoyer, S. & Hamman, J. J. xarray: N-D labeled Arrays and Datasets in Python. *Journal of Open Research Software* **5**, doi:10.5334/jors.148 (2017).

90   Šavrič, B., Patterson, T. & Jenny, B. The Equal Earth map projection. *International Journal of Geographical Information Science* **33**, 454-465, doi:10.1080/13658816.2018.1504949 (2018).

Figures
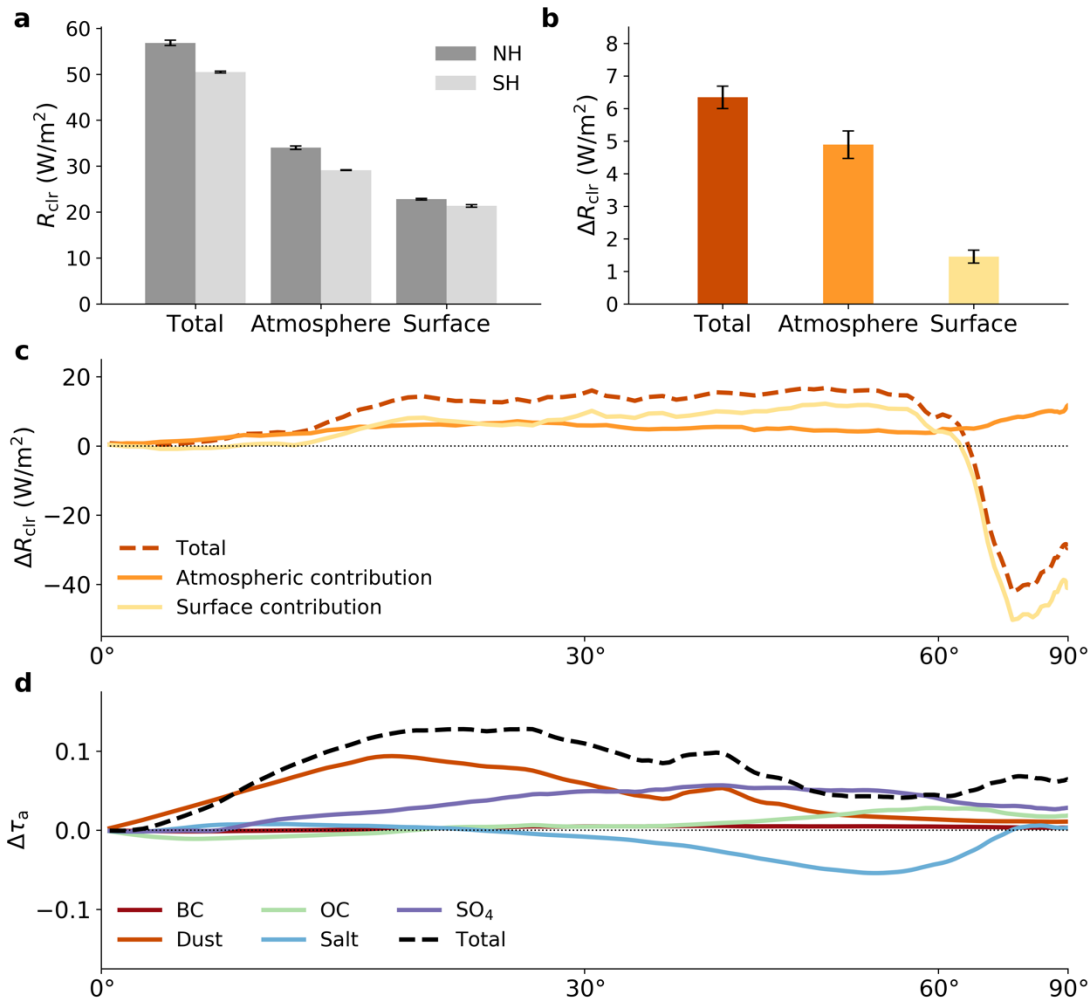
Fig. 1 | The atmosphere, not the surface, contributes most to the observed clear-sky hemispheric albedo asymmetry. a-c, Hemispherically-averaged clear-sky reflected solar radiation (**a**), the hemispheric difference (Northern Hemisphere minus Southern Hemisphere) (**b**), and zonal differences (**c**). **d**, Zonal hemispheric difference for total AOD and each species. Error bars in **a-b** represent 95% confidence in the mean value. For **c-d**, the abscissa is area-weighted (plotted as sine of latitude). All averages are for 2003-2020, inclusive.
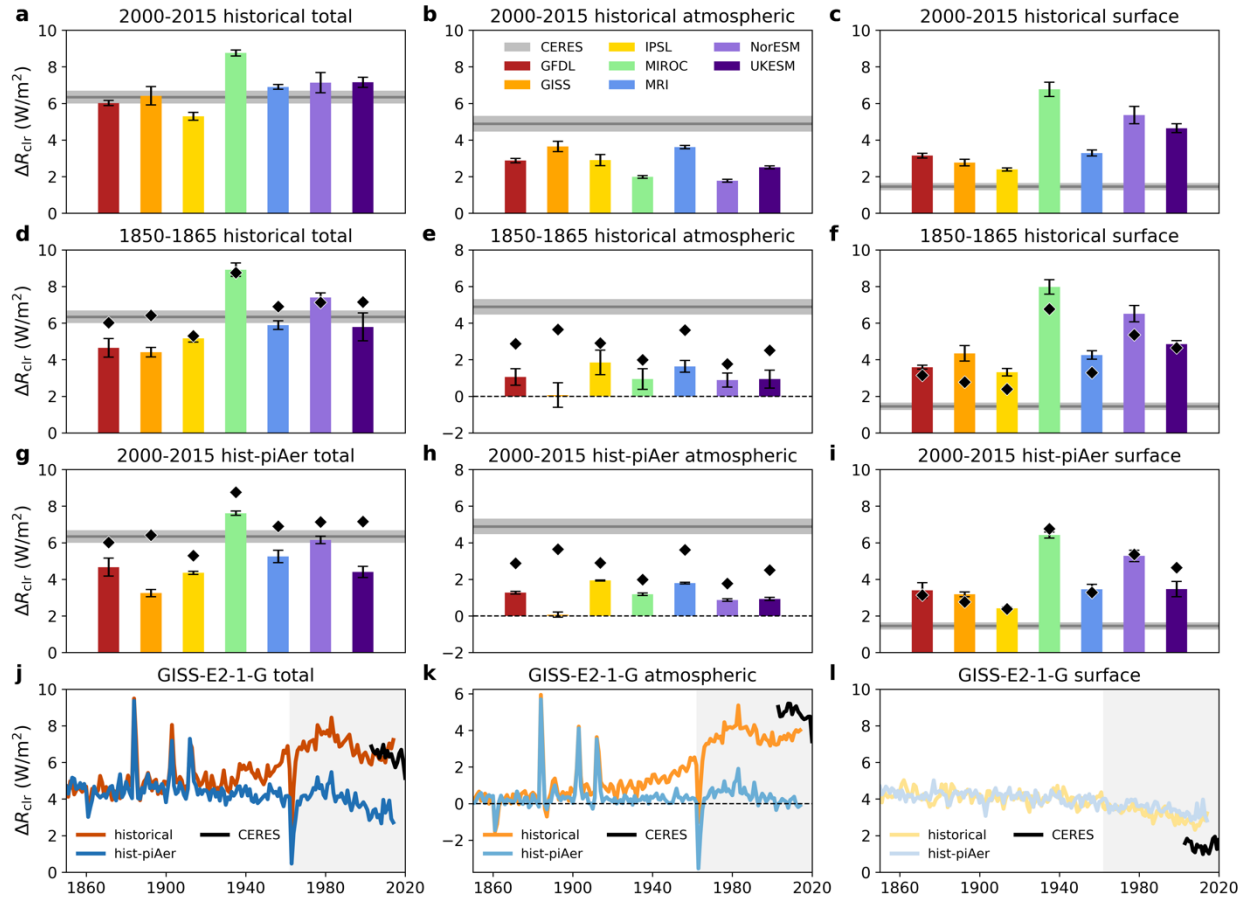
Fig. 2 | Clear-sky hemispheric albedo asymmetry changes in historical CMIP6 runs.
Average of the Northern Hemisphere minus Southern Hemisphere total clear-sky reflection and its atmospheric and surface contributions for the 2000-2015 period in the historical runs (**a-c**), 1850-1865 period in the historical runs (**d-f**), and 2000-2015 in the hist-piAer runs (**g-i**). Error bars for each model represent 95% confidence in the mean value. Diamond markers in **d-i** represent each model's 2000-2015 historical run mean value for reference. CERES mean values are shown as gray lines with shading representing the 95% confidence interval. **j-l**, Example time series of historical and hist-piAer total, atmospheric, and surface reflection asymmetries from the GISS-E2-1-G model. Shading represents the time period in which reliable space-based estimates of Earth's albedo have been available.
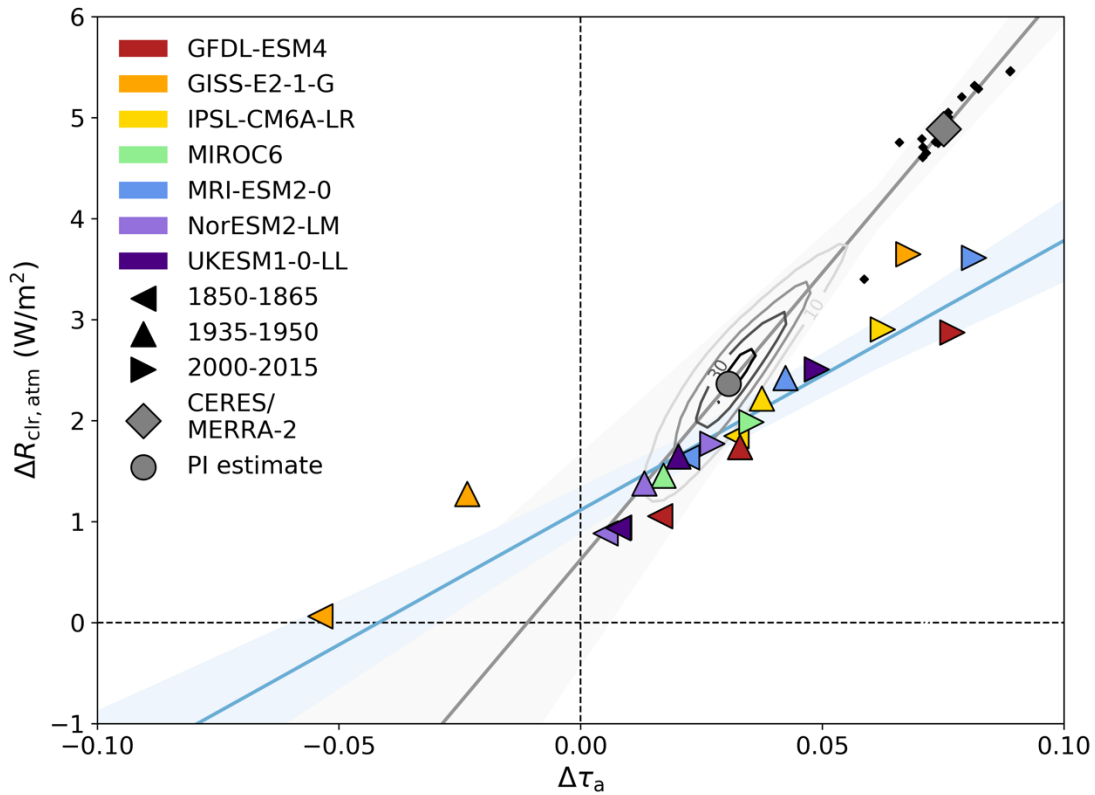
Fig. 3 | Relationship between the hemispheric aerosol and atmospheric reflection asymmetries in the pre-industrial, midcentury, and present-day. CMIP6 model values from the historical runs are represented as colored triangles (facing left for the 1850-1865 mean, up for 1935-1950, right for 2000-2015) and their regression fit and its 95% confidence interval are represented by the blue line and shading. CERES/MERRA-2 data are represented as a gray diamond for the modern mean and as smaller black diamonds for individual years. The regression fit between individual CERES/MERRA-2 years and its 95% confidence interval is represented by the gray line and shading. Contours represent kernel density estimates of the Monte Carlo probabilities (shown every 10 counts) for calculating the pre-industrial value of $\Delta R_{clr,atm}$, with the gray circle representing the mean value.
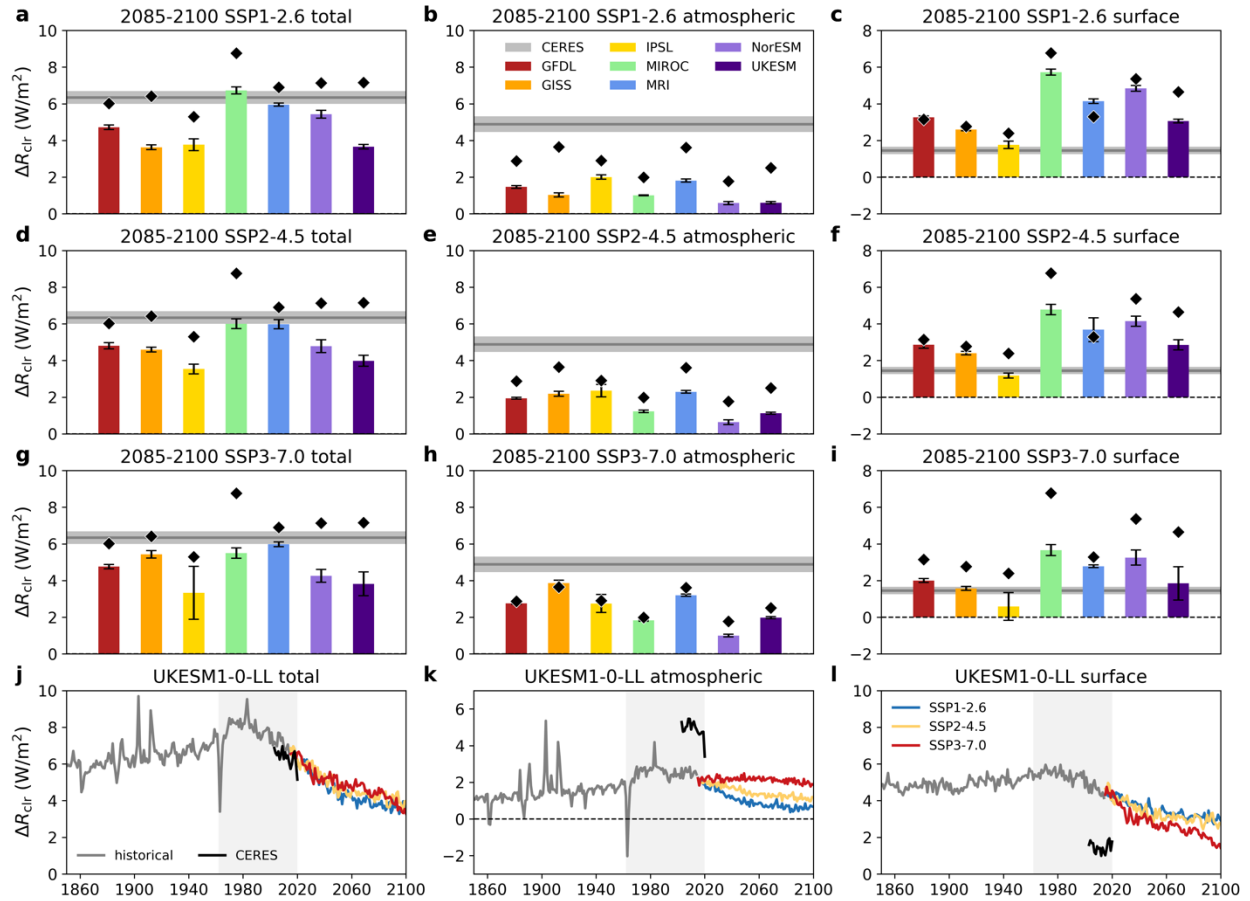
Fig. 4 | Clear-sky hemispheric albedo asymmetry changes in CMIP6 runs of future scenarios. a-i, as in Fig. 2 d-i, but for the SSP1-2.6 (**a-c**), SSP2-4.5 (**d-f**), and SSP3-7.0 (**g-i**) runs. **j-l**, as in Fig. 2 j-l, but for the UKESM1-0-LL model.
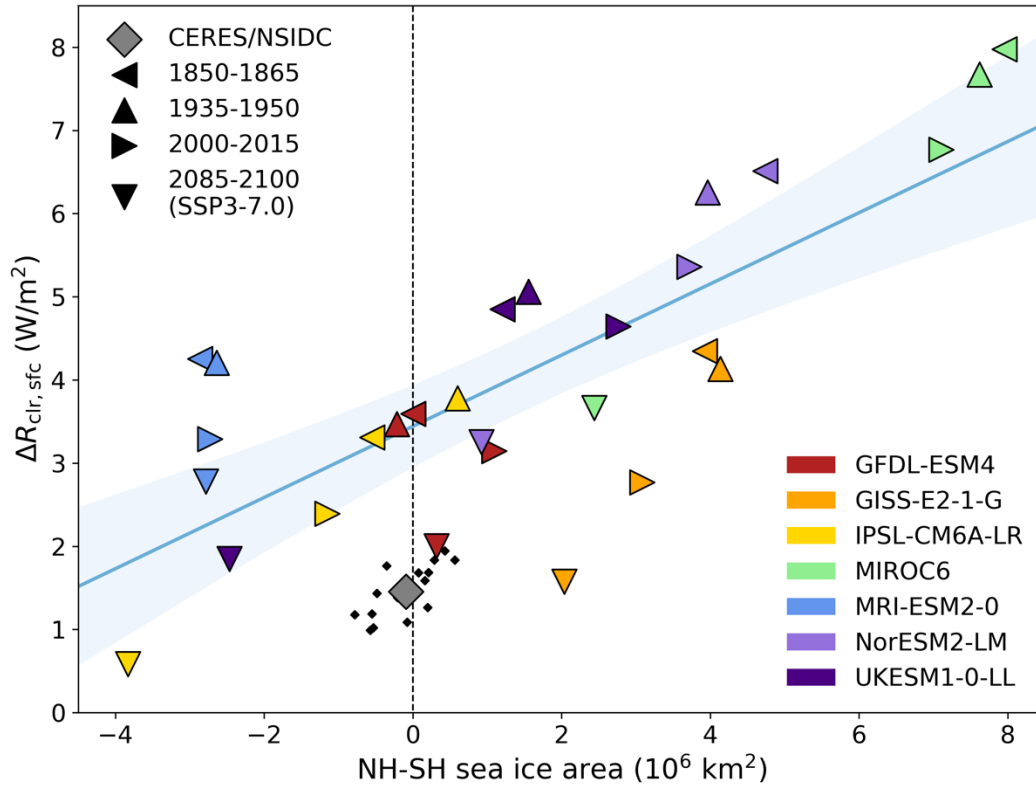
Fig. 5 | Relationship between the hemispheric sea ice and surface reflection asymmetries in the pre-industrial, midcentury, present-day, and high-emissions future. CMIP6 model values from the historical and SSP3-7.0 runs are represented as colored triangles (facing left for the 1850-1865 mean, up for 1935-1950, right for 2000-2015, down for 2085-2100) and their regression fit and its 95% confidence interval are represented by the blue line and shading. CERES/National Snow and Ice Data Center (NSIDC) data are represented as a gray diamond for the modern mean and as smaller black diamonds for individual years.

Extended Data
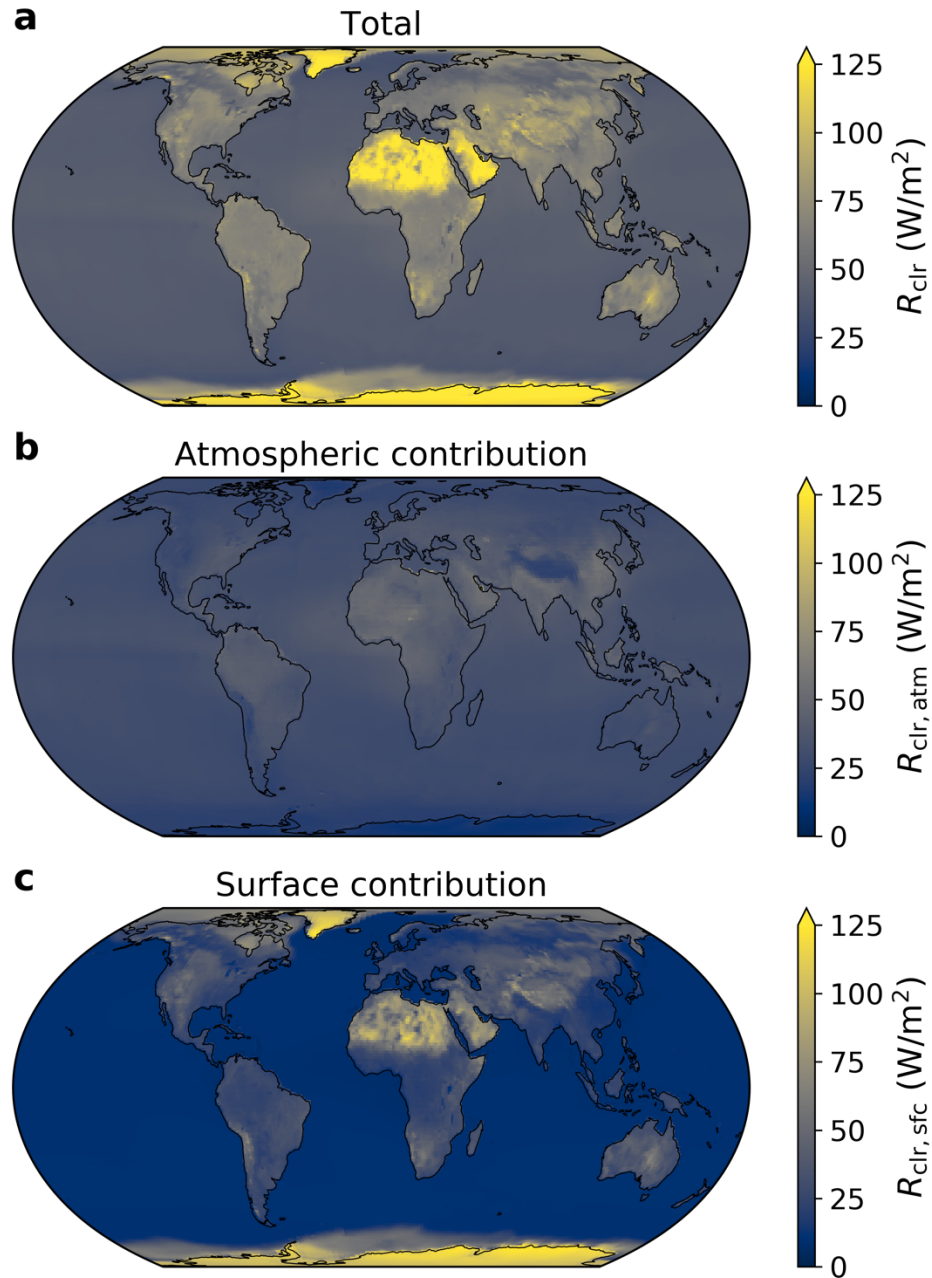
Extended Data Fig. 1 | Maps of clear-sky reflection. Total R_{clr} (**a**) and its atmospheric (**b**) and surface (**c**) components are shown globally on an equal-area projection[90].
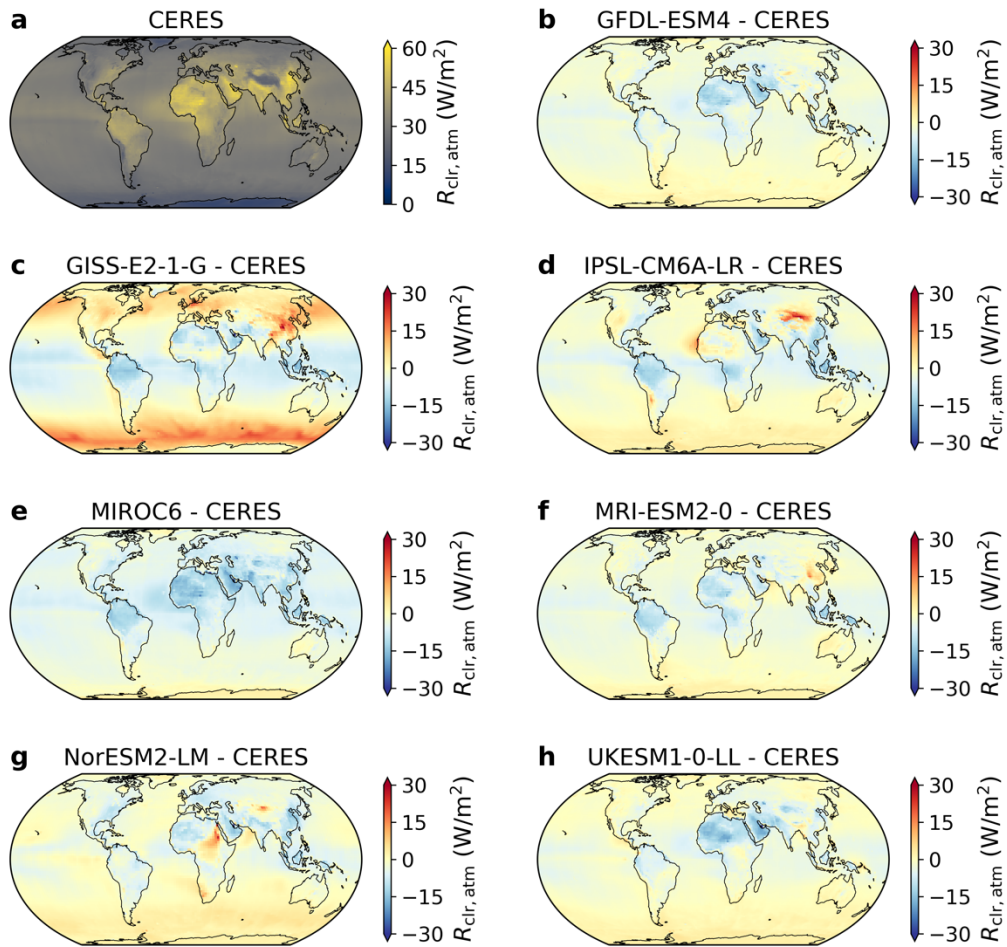
Extended Data Fig. 2 | Maps of the atmospheric contribution to clear-sky reflection for CERES and the CMIP6 models. Observed $R_{clr,atm}$ from CERES (**a**) and the difference between the observed value and each of the CMIP6 models analyzed (**b-h**) are shown globally on an equal-area projection[90].
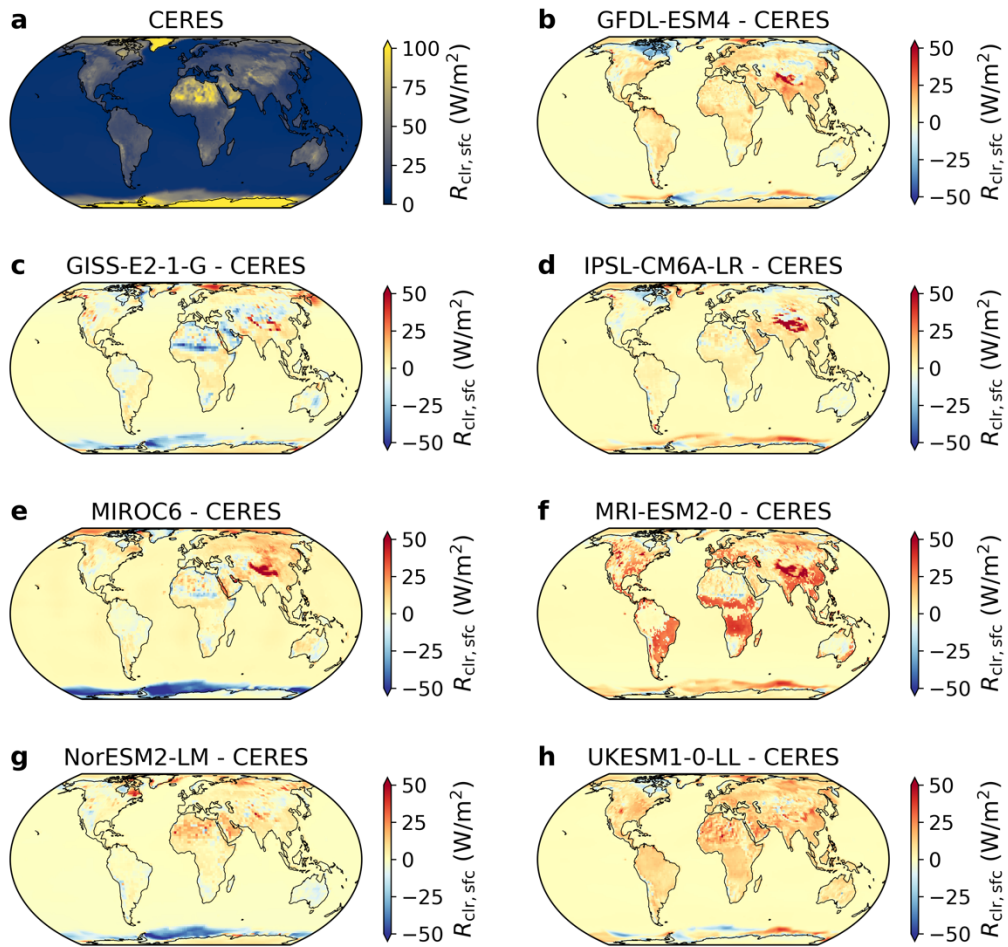
Extended Data Fig. 3 | Maps of the surface contribution to clear-sky reflection for CERES and the CMIP6 models. Observed $R_{\text{clr,sfc}}$ from CERES (**a**) and the difference between the observed value and each of the CMIP6 models analyzed (**b-h**) are shown globally on an equal-area projection[90].
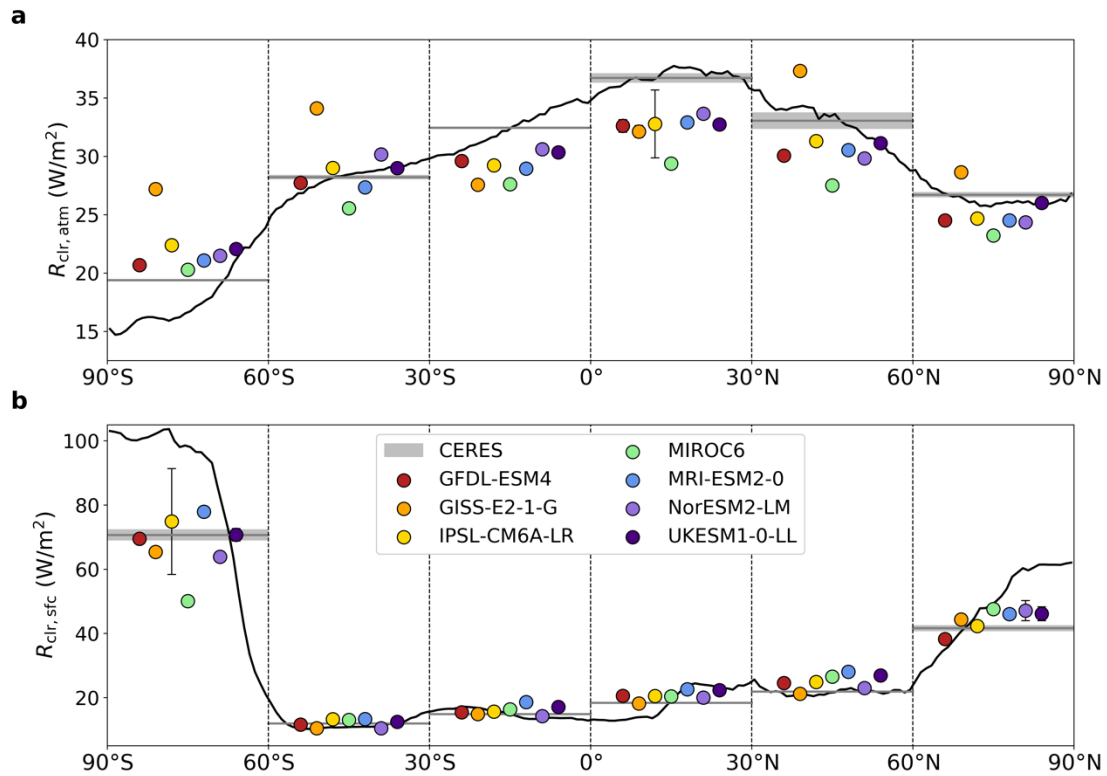
Extended Data Fig. 4 | Zonal differences between CERES and the CMIP6 observations. a, mean CERES value and 95% confidence interval are represented by the gray line and shading and mean CMIP6 model value and 95% confidence interval are represented by the circular markers and error bars for the atmospheric component of the clear-sky reflection for the Southern Hemisphere poles (90°-60° S), midlatitudes (60°-30° S), and tropics (30° S-0°) and the Northern Hemisphere tropics (0°-30° N), midlatitudes (30°-60° N), and poles (60°-90° N). Zonal mean CERES observations are shown as a dark gray line for reference. **b**, as in **a**, but for the surface component of the clear-sky reflection. Large errors for IPSL-CM6A-LR in the Northern Hemisphere tropics and Southern Hemisphere poles are primarily due to a very high degree of temporal autocorrelation as opposed to large standard deviations.
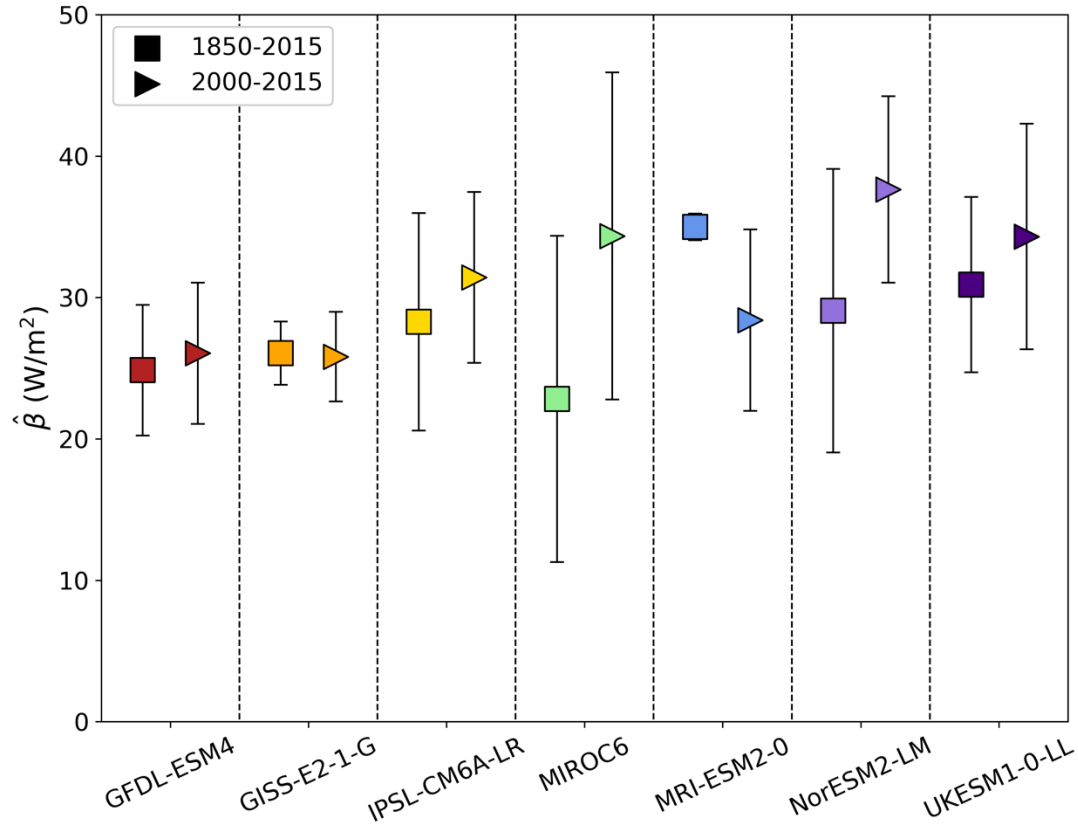
Extended Data Fig. 5 | Modern and full historical regression slopes for each CMIP6 model.
Regression slopes ($\hat{\beta}$, units of W/m^2 in $\Delta R_{clr,atm}$ per unit $\Delta\tau_a$) for each CMIP6 model and their 95% confidence intervals are represented by colored markers (square for the 1850-2015 regression, triangle for 2000-2015 only) and error bars.
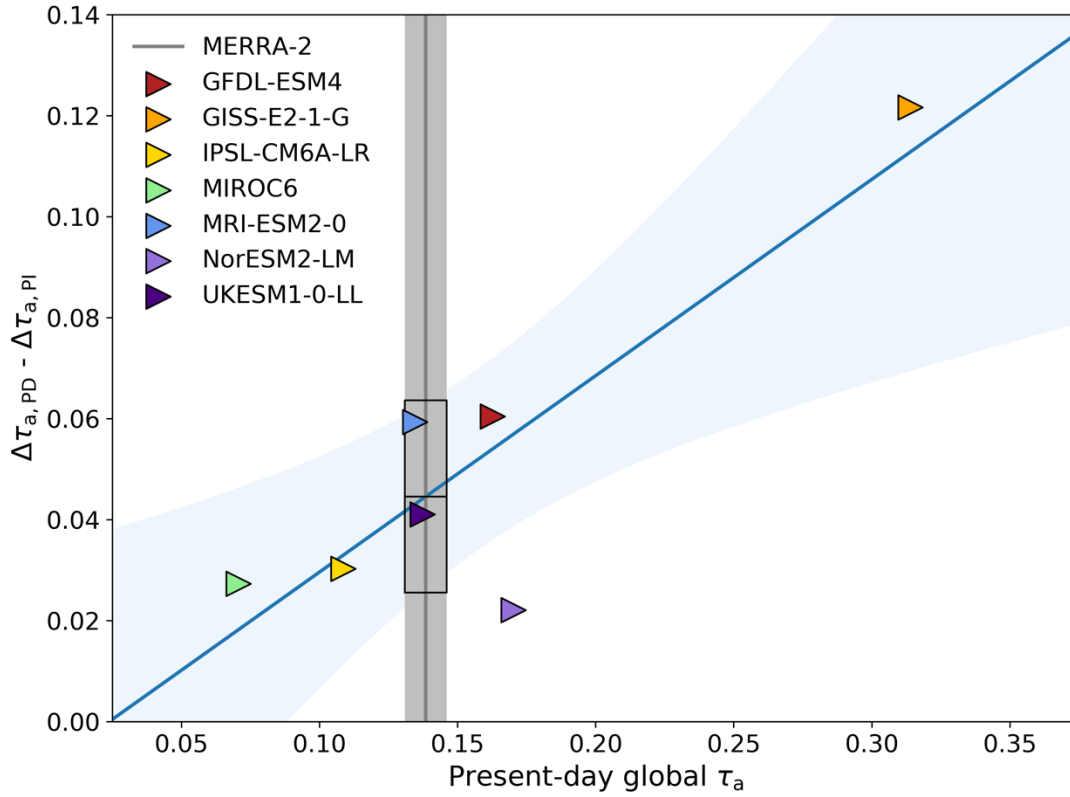
Extended Data Fig. 6 | Emergent constraint for the change in hemispheric aerosol contrast from present-day to pre-industrial based on present-day global mean aerosol optical depth. CMIP6 models are represented by the colored triangles and their regression slope and its 95% confidence interval by the blue line and shading. MERRA-2 values for the present-day global mean AOD and its 95% confidence interval are represented by the gray line and shading. The constraint on the present-day to pre-industrial change in $\Delta\tau_a$ is represented by the black box, with a center line at the mean value and extent based on the 95% confidence interval.

SSP3-7.0 2085-2100 minus historical 2000-2015
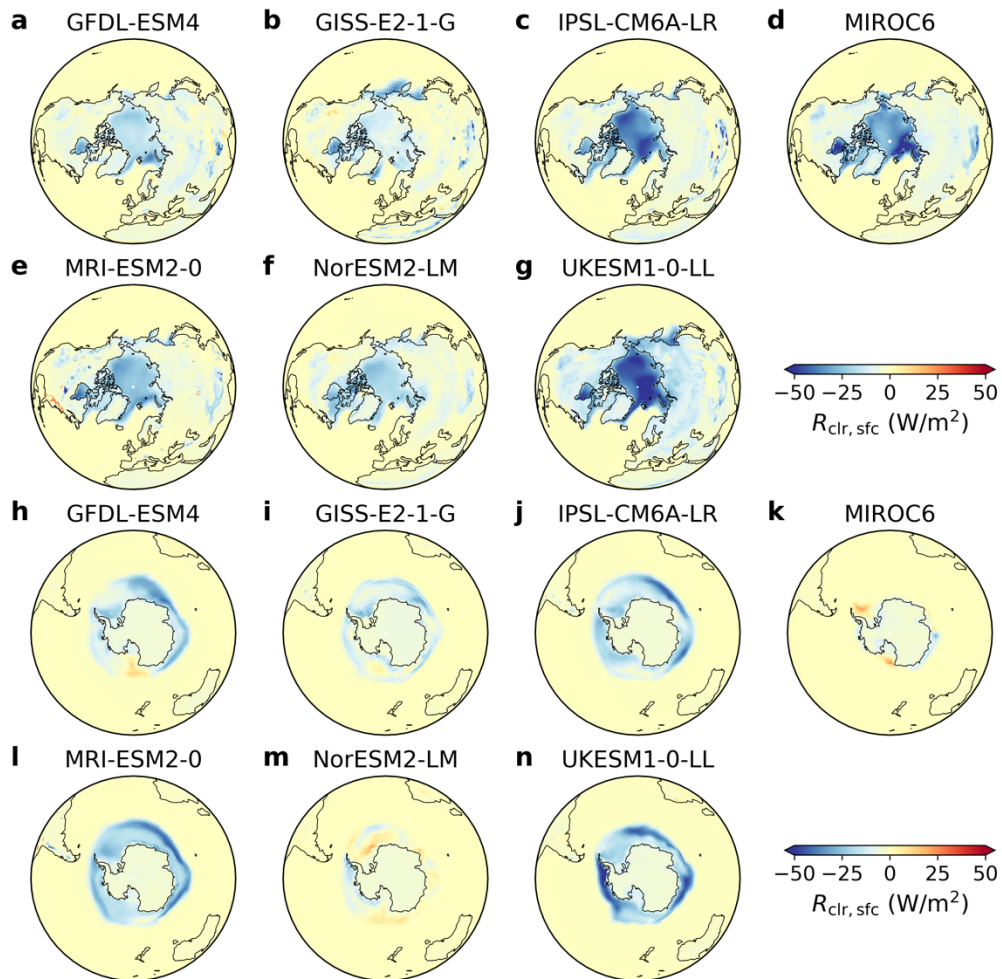
Extended Data Fig. 7 | Change in surface reflection over the poles in the SSP3-7.0 high-emissions scenario. Difference in surface reflection between the SSP3-7.0 end-of-century (2085-2100 mean) and historical present-day (2000-2015 mean) for each CMIP6 model centered around the Arctic (**a-g**) and Antarctic (**h-n**) using an orthographic map projection.
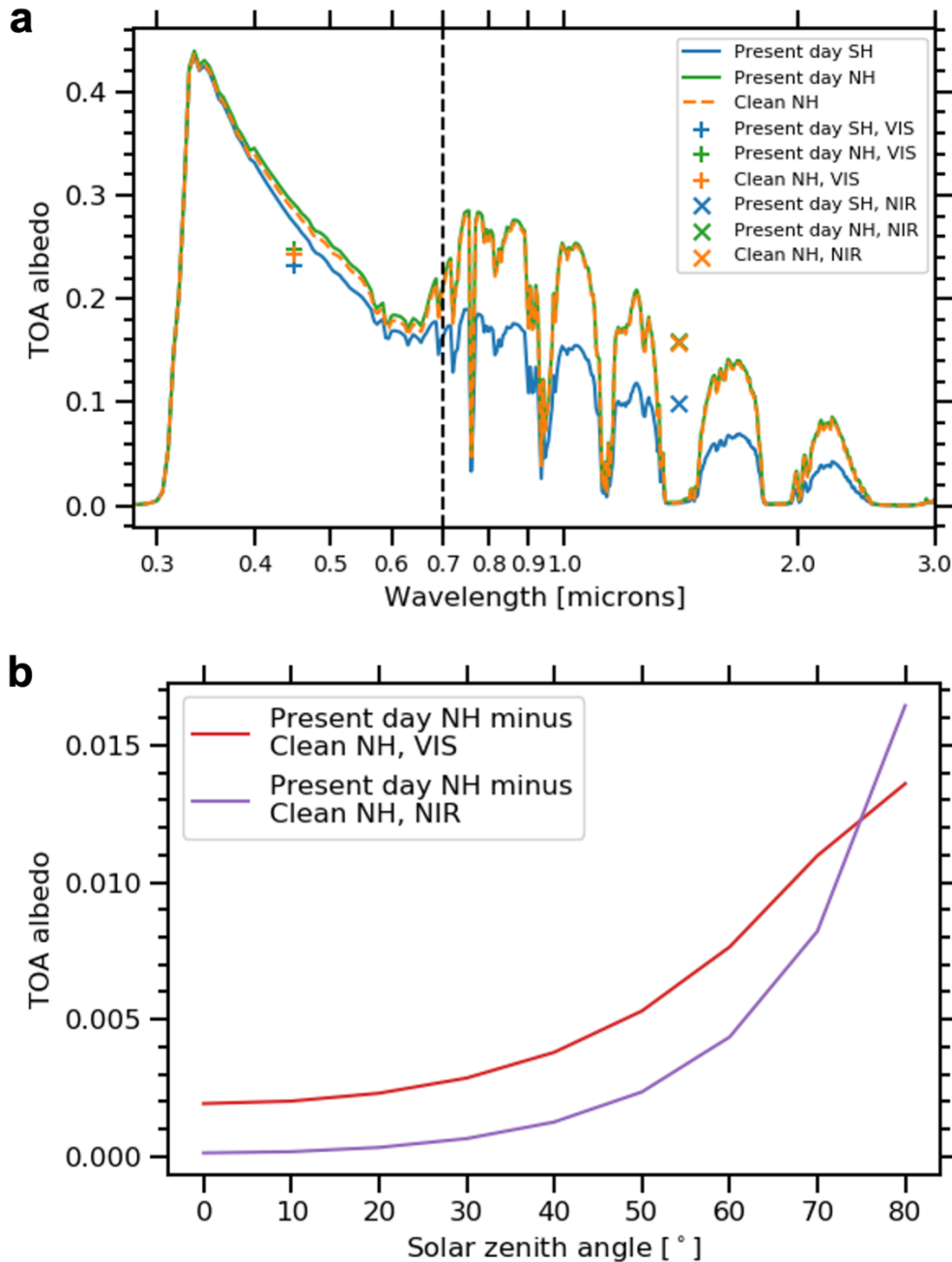
Extended Data Fig. 8 | Radiative transfer calculations of the clear-sky albedo for a hypothetical "cleaner" Northern Hemisphere. a, spectral top-of-atmosphere albedo at an example solar zenith angle of 50° for present-day Norther Hemisphere, present-day Southern Hemisphere, and clean Northern Hemisphere. Spectrally-integrated albedos for the ultraviolet and visible portion (VIS) of the spectrum (0.2-0.7 μm) are represented by the colored pluses and the near-infrared portion (NIR) of the spectrum (0.7-3.0 μm) by crosses. **b**, differences between present-day and clean NH for VIS and NIR albedo as a function of solar zenith angle.